# The Effect of Torsional Motion on Multiexciton Formation through Intramolecular Singlet Fission in Ferrocene-Bridged Pentacene Dimers

Hayasaka, Ryo ; Sakai, Hayato ; Fuki, Masaaki ; Okamoto, Tsubasa ; Khan, Ramsha ; Higashi, Masahiro ; Tkachenko, Nikolai V. ; Kobori,…

(Citation)
Angewandte Chemie International Edition,63(8):e202315747

(Issue Date)
2024-02-19

(Resource Type)
journal article

(Version)
Version of Record



(URL)
https://hdl.handle.net/20.500.14094/0100487510

How to cite: *Angew. Chem. Int. Ed.* **2024**, *63*, e202315747
doi.org/10.1002/anie.202315747

Photochemistry

# The Effect of Torsional Motion on Multiexciton Formation through Intramolecular Singlet Fission in Ferrocene-Bridged Pentacene Dimers

*Ryo Hayasaka, Hayato Sakai, Masaaki Fuki, Tsubasa Okamoto, Ramsha Khan, Masahiro Higashi, Nikolai V. Tkachenko,* Yasuhiro Kobori,* and Taku Hasobe**

**Abstract:** A series of ferrocene(Fc)-bridged pentacene-(Pc)-dimers [Fc–Ph(2,*n*)–$(Pc)_2$: *n* = number of phenylene spacers] were synthesized to examine the tortional motion effect of Fc-terminated phenylene linkers on strongly coupled quintet multiexciton ($^5$TT) formation through intramolecular singlet fission (ISF). Fc–Ph-(2,4)–$(Pc)_2$ has a relatively small electronic coupling and large conformational flexibility according to spectroscopic and theoretical analyses. Fc–Ph(2,4)–$(Pc)_2$ exhibits a high-yield $^5$TT together with quantitative singlet TT ($^1$TT) generation through ISF. This demonstrates a much more efficient ISF than those of other less flexible Pc dimers. The activation entropy in $^1$TT spin conversion of Fc–Ph(2,4)–$(Pc)_2$ is larger than those of the other systems due to the larger conformational flexibility associated with the torsional motion of the linkers. The torsional motion of linkers in $^1$TT is attributable to weakened metal-ligand bonding in the Fc due to hybridization of the hole level of Pc to Fc in $^1$TT unpaired orbitals.

[*] R. Hayasaka, Dr. H. Sakai, Prof. Dr. T. Hasobe
Department of Chemistry, Faculty of Science and Technology, Keio University
Yokohama, Kanagawa 223–8522 (Japan)
E-mail: hasobe@chem.keio.ac.jp
Dr. M. Fuki, Dr. T. Okamoto, Prof. Dr. Y. Kobori
Molecular Photoscience Research Center, Kobe University
1-1 Rokkodai-cho, Nada-ku, Kobe 657–8501 (Japan)
and
Department of Chemistry, Graduate School of Science, Kobe University
1-1, Rokkodai-cho, Nada-ku, Kobe 657-8501 (Japan)
and
CREST, JST
Honcho 4-1-8, Kawaguchi, Saitama 332-0012 (Japan)
E-mail: ykobori@kitty.kobe-u.ac.jp
R. Khan, Prof. Dr. N. V. Tkachenko
Chemistry and Advanced Materials Group, Faculty of Engineering and Natural Sciences, Tampere University
Korkeakoulunkatu 8, 33720 Tampere (Finland)
E-mail: nikolai.tkachenko@tuni.fi
Prof. Dr. M. Higashi
Department of Complex Systems Science, Graduate School of Informatics, Nagoya University
Furo-cho, Chikusa-ku, Nagoya 464-8601 (Japan)



## Introduction

Molecular machinery involving rotational motion is an essential process in nearly all living systems, from energy production and transport to muscle.[1] Inspired by such fascinating functions and processes in natural systems, a variety of artificial molecular machine has been synthesized to date, and some of which exhibit complicated mechanical behaviors and demonstrated potential applications in future responsive molecular devices and smart materials.[2]

Metallocene is a well-known molecule which can be a component of molecular rotors due to its favorable thermodynamic properties of coordination bonds.[2a] Ferrocene (Fc) is the most commonly used because it has a structure in which an iron (II) ion is sandwiched between two freely rotating cyclopentadienyl rings with a small rotational barrier (3.8 kJ mol$^{-1}$).[3] A number of molecular rotors using 1,1′-disubstituted ferrocene have been reported, which can control rotational motion and conformation in response to external stimuli such as light,[4] redox[5] and supramolecular interactions.[6]

Singlet fission (SF) is a spin-allowed multiexciton generation process in which two uncoupled triplet excitons (T + T) are generated through a correlated triplet pair (TT) from one-photon absorption in two nearby molecules ($S_1$ + $S_0$), as shown in eq. 1.[7]

$$S_1 + S_0 \rightarrow TT \rightarrow T + T \quad (1)$$

The energy matching condition between the lowest-lying singlet excited state [$E(S_1)$] and two triplet excited state [$E(T_1)$] [i.e., $E(S_1) \geq 2E(T_1)$] is required for SF. Pentacene (Pc) satisfied the condition [$E(S_1)$: 2.1 eV, $E(T_1)$: 0.8 eV].[8] Therefore, intramolecular SF (ISF) of Pc-dimers whose distance and orientation are controlled by covalent linkers have been intensively investigated.[9] Recently, we proposed a molecular design strategy for quantitative T + T through ISF using a series of acene-dimers.[10] In addition to the conventional "electronic coupling" associated with ISF rate constants, "conformational flexibility" is essential for TT

 

dissociation because of the structural change from planar TT to distorted T+T estimated by time-resolved electron paramagnetic resonance (TREPR).[10a,11] In contrast, when an inflexible xanthene-bridged Pc-dimer was employed, TT was formed quantitatively in solution due to the strong chromophore coupling, but no T+T were produced.[9e] Note that there is also another approach utilizing an energetic driving force for TT dissociation.[12]

In addition to the increased efficiencies of SF-based photovoltaics associated with the increased excitons,[13] the quintet TT [($^5$TT)] may reduce losses in photovoltaics because the direct decay from ($^5$TT) to the singlet ground state is doubly spin-forbidden.[14] ($^5$TT) consist of four quantum entangled spins and are promising for quantum information science.[15] Although the dynamics of singlet and quintet TT ($^1$TT and $^5$TT) have been discussed extensively, most of them have been observed by TREPR under cryogenic conditions, and no evaluation under the same conditions with transient absorption (TA) has been made except for limited examples by us.[10b] To observe high-yield and long-lived TT, it is essential to control the orientation of two chromophores in $^5$TT due to the conformational change after photoexcitation, which is extremely difficult to achieve with conventional covalent dimers. To facilitate the above conformational changes, a synthetic strategy is to use dimers with rotational units, but so far no such examples have been reported.

As shown in Figure 1, structural parameters such as spacer length: *n* and rotational Fc for control of electronic coupling and conformational flexibility were arranged. Herein, a series of Fc-terminated phenylene-bridged Pc-dimers were newly synthesized [denoted as Fc–Ph(2,*n*)–(Pc)$_2$: *n* shows the number of phenylene spacers linked at 1 or 1′ positions of Fc (*n*=2: homo-dimer, *n*=3,4: hetero-dimer)] together with Xan-bridged Pc-dimers without a rotational unit [Xan–Ph(2,*n*)–(Pc)$_2$: *n*=3,4], reference Fc-terminated phenylene-bridged Pc-monomers [Fc–Ph(*n*)–Pc: *n*=0,1,2,3] and pristine Pc-monomer (Pc-ref). Note that Fc–Ph(*n*)–Pc were used to evaluate the rate constants of intersystem crossing (ISC) due to the heavy-atom effects between Fc and Pc. Finally, we have successfully observed the quantitative $^1$TT generation ($\Phi_{1TT}$: 100 %) and high-yield $^5$TT ($\Phi_{5TT}$: 55 %) in Fc–Ph(2,4)–(Pc)$_2$ by changing the *n*.

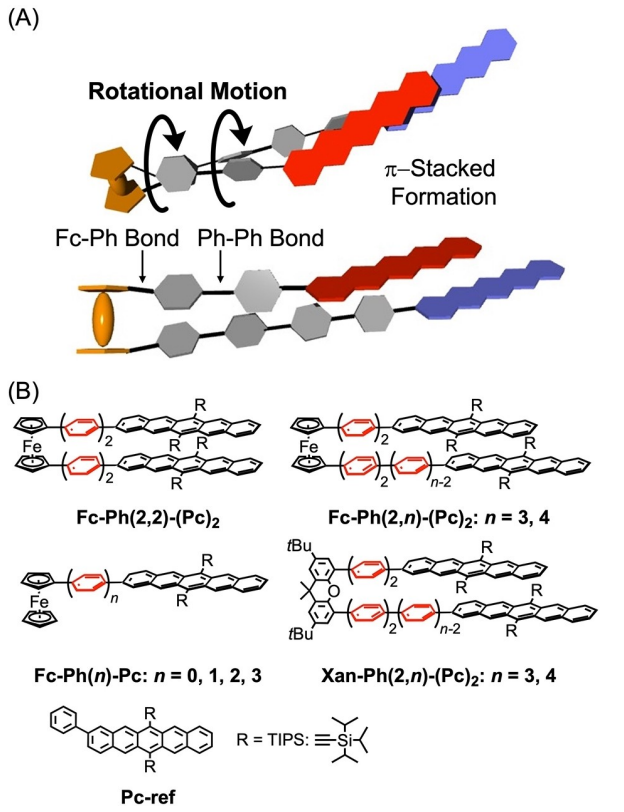


***Figure 1.*** (A) Schematic illustrations of Fc–Ph(2,*n*)–(Pc)$_2$. The gray and brown show phenylene and ferrocene units together with pentacenes (blue and red). The torsional motions of Fc-phenylene bond (Fc–Ph) and phenylene-phenylene bond (Ph–Ph) associated with the rotation of Fc is described. (B) Chemical structures of Pc-derivatives in this study.

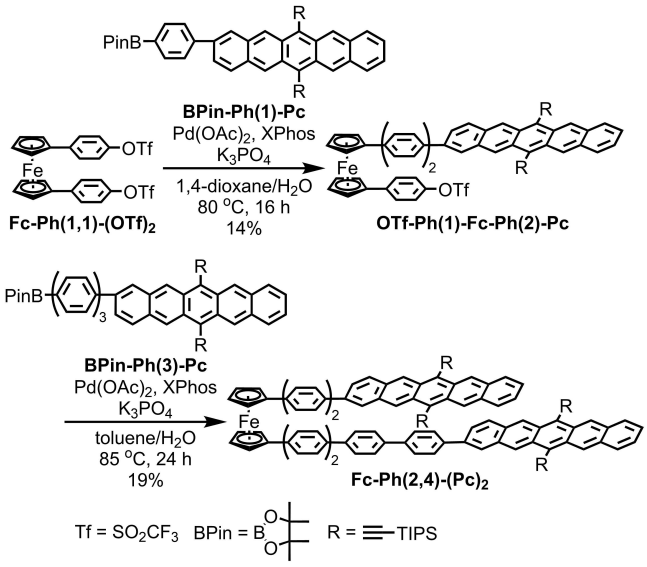


***Scheme 1.*** Synthetic Scheme of Fc–Ph(2,4)–(Pc)$_2$.

## *Results and Discussion*

The detail synthetic procedures of these compounds are described in Scheme 1 and Schemes S1–S6 in Supporting Information. Briefly, synthesis of Fc–Ph(2,4)–(Pc)$_2$ was performed by two step Suzuki–Miyaura cross-coupling of Fc–Ph(1,1)–(OTf)$_2$ with BPin–Ph(1)–Pc and BPin–Ph(3)–Pc via an intermediate: OTf–Ph(1)–Fc–Ph(2)–Pc All isolated compounds were successfully characterized (Figures S1–S63).

First, we performed photophysical evaluations of Fc–Ph(*n*)–Pc to examine the heavy-atom effect on the lifetimes of singlet excited-state of Pc ($^1$Pc*). It was evident that when the *n* is greater than or equal to 2, the quenching of $^1$Pc* due to the heavy-atom effect can be neglected (Figures S64–S79, Tables S1–S3, Scheme S7) because the ISF rate constants are much larger than those of ISC. Therefore, two or more

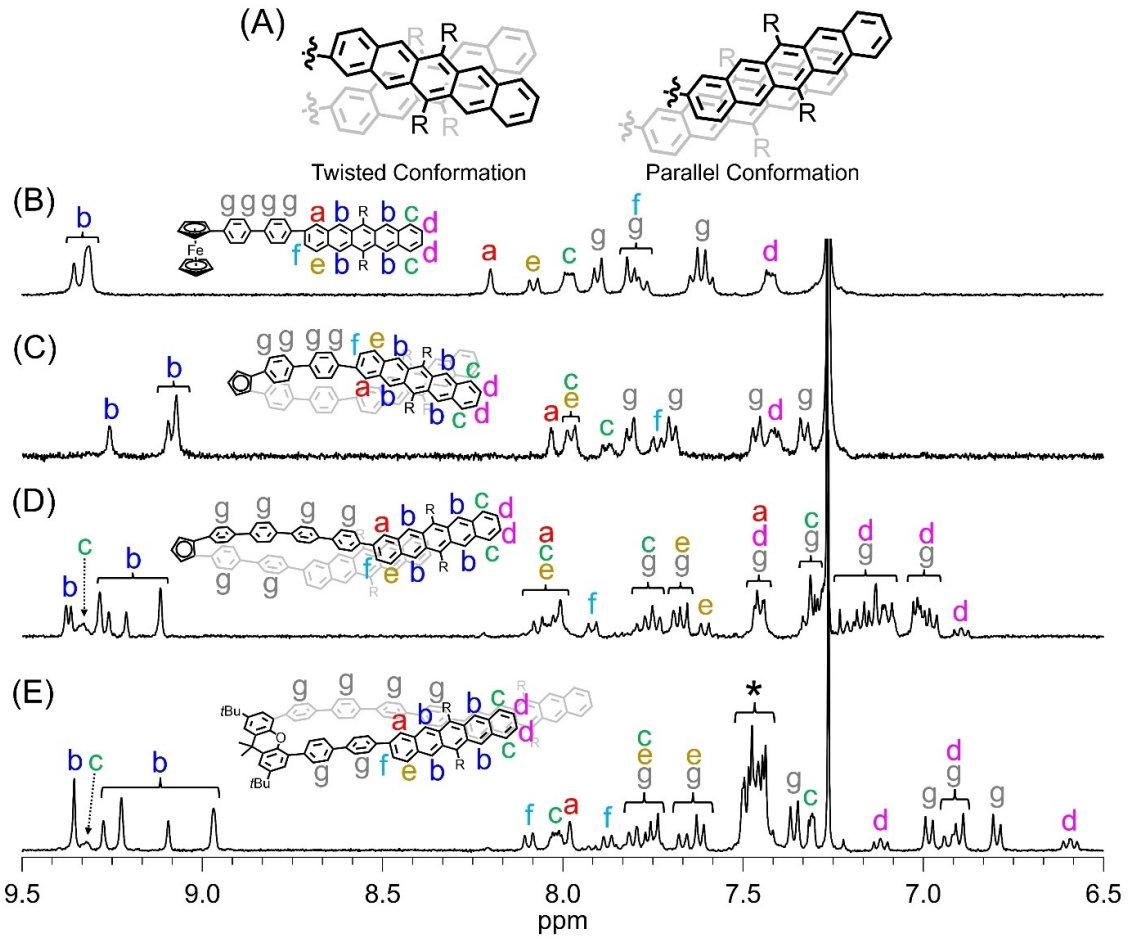


***Figure 2.*** (A) Schematic view of twisted and parallel conformations of two Pc units in Fc–Ph(2,*n*)–$(Pc)_2$. $^1$H NMR spectra of (B) Fc–Ph(2)–Pc, (C) Fc–Ph(2,2)–$(Pc)_2$, (D) Fc–Ph(2,4)–$(Pc)_2$, and (E) Xan–Ph(2,4)–$(Pc)_2$. The asterisk (*) shows multiplet signals composed of the protons corresponding to a, d, g and xanthene units.

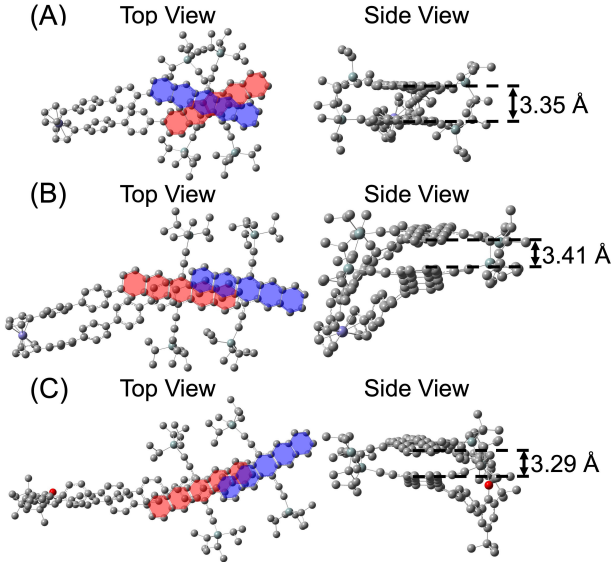


***Figure 3.*** Optimized structures of (A) Fc–Ph(2,2)–$(Pc)_2$, (B) Fc–Ph(2,4)–$(Pc)_2$, and (C) Xan–Ph(2,4)–$(Pc)_2$ calculated by DFT method at B3LYP–D3/6–311G(d) level. The hydrogen atoms are omitted for simplicity.

phenylene units ($n$ = 2,3,4) were employed as a spacer in the synthesis of Fc-bridged Pc-dimers.

To discuss the structural conformations between two Pc units, we systematically performed $^1$H NMR measurements (Figures 2, S80) and density function theory (DFT) calculations at the B3LYP-D3/6-311G(d) level (Figures 3, S81–S82). As shown in $^1$H NMR spectra of these Pc-dimers and reference monomers, peak signals derived from phenylene and Pc units were observed in the range of ca. 6.5–9.5 ppm in $^1$H NMR spectra. The proton peaks of Pc units in all Fc–Ph(2,*n*)–$(Pc)_2$ were significantly upfilled shifted as compared to Fc–Ph(2)–Pc. According to previous $^1$H NMR studies,[5b,c,6a,b] the up-field shift of the aromatic units introduced at the 1,1′ positions of Fc is due to the interactions between Pc units, which favors the formation of *syn*-like conformations (closed form) between the aromatic units.

It should be noted, that in closed form we can consider two different conformations of two Pc units such as twisted and parallel conformations (Figure 2A). The optimized structures of these Pc-dimers were estimated as shown in Figure 3 and Figures S81–S82. In Fc–Ph(2,2)–$(Pc)_2$, the twisted conformation is more stable than the parallel

conformation by 28 kJ mol$^{-1}$ because of the large steric hindrance of TIPS-substituents (Figure 3A). This is in sharp contrast with Fc–Ph(2,4)–(Pc)$_2$ (Figure 3B) and Fc–Ph-(2,3)–(Pc)$_2$ (Figure S80A), which result in a more stable parallel conformation because the steric hindrance between TIPS-substituents is reduced by the asymmetric introduction of phenylene spacers.

By once again focusing on the $^1$H NMR results of Fc–Ph(2)–Pc and Fc–Ph(2,2)–(Pc)$_2$ (Figures 2B–2 C), the signal patterns of Fc–Ph(2,2)–(Pc)$_2$ are in good agreement with those of Fc–Ph(2)–Pc. The Pc units are symmetrically arranged via a linker and the protons are equivalently observed. A new peak corresponding to proton c appeared at ≈7.9 ppm in Fc–Ph(2,2)–(Pc)$_2$ because the proton c is strongly affected by the aromatic ring current effect from the other Pc. Additionally, the signals of protons e and f are not affected by the ring current effect and are not significantly shifted. Considering the above, two Pc units in Fc–Ph(2,2)–(Pc)$_2$ show the parallel conformation, which is in good agreement with the above-discussions by DFT. In contrast, in Fc–Ph(2,4)–(Pc)$_2$ (Figure 2D), new up-field shift protons of the Pc unit, such as protons b-f were detected, which were not observed in Fc–Ph(2,2)–(Pc)$_2$. The low-field shift of proton c was seen at 9.3 ppm because of the deshielding effect from the other Pc. Based on the above, we can conclude that Fc–Ph(2,4)–(Pc)$_2$ has the parallel conformation in contrast with the twisted conformation of Fc–Ph(2,2)–(Pc)$_2$. Additionally, the peak patterns of Pc in Xan–Ph(2,4)–(Pc)$_2$ are in good agreement with those of Fc–Ph(2,4)–(Pc)$_2$ (Figures 2D–2E, S80).

Then, steady-state spectroscopic measurements were performed to examine the electronic properties (Figures 4, S83–S85). First, it should be noted that toluene (less-polar solvent) was used as the solvent to eliminate the unexpected

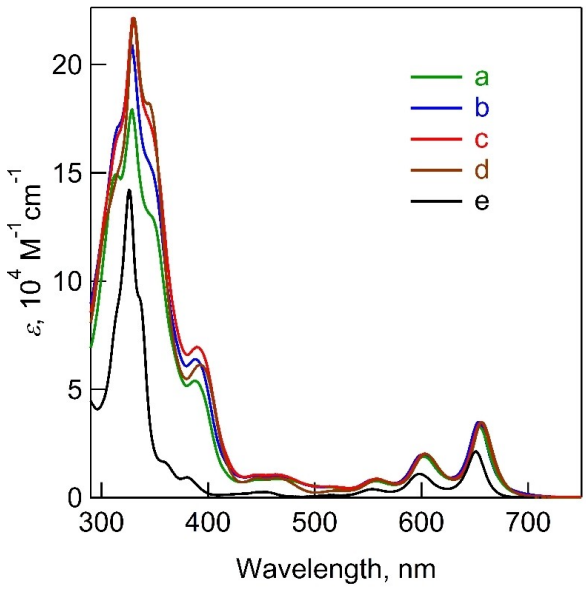


***Figure 4.*** Absorption spectra of (a) Fc–Ph(2,2)–(Pc)$_2$, (b) Fc–Ph(2,3)–(Pc)$_2$, (c) Fc–Ph(2,4)–(Pc)$_2$, (d) Xan–Ph(2,4)–(Pc)$_2$ and (e) Pc-ref in toluene.

electron transfer from Fc to $^1$Pc*. The detail energetic estimations are shown in Table S4. Absorption spectra of these compounds are shown in Figures 4, S83. The spectra of Fc–Ph(2,*n*)–(Pc)$_2$ (spectra a-c in Figure 4) and Xan–Ph-(2,4)–(Pc)$_2$ (spectrum d) became red-shifted and broadened as compared to that of Pc-ref (spectrum e) because of the electronic interaction between two Pc units and phenylene spacers. The molar absorption coefficients ($\varepsilon$) of these Pc-dimers significantly increased as compared to Pc-ref because of the dimeric form (Table S5). The spectral shape of Fc–Ph(2,4)–(Pc)$_2$ (spectrum c) agrees well with that of Xan–Ph(2,4)–(Pc)$_2$ (spectrum d). This means the quite similar conformation of two Pc units through spacers. Furthermore, the split and broader absorption bands of Fc–Ph(2,*n*)–(Pc)$_2$ in the range of 300–400 nm relative to Pc-ref should be ascribed to the dipole-dipole interactions between two Pc chromophores. The splitting energies ($\Delta$DS) derived from Davydov splitting were estimated to be 1260 cm$^{-1}$ for Fc–Ph(2,2)–(Pc)$_2$, 1120 cm$^{-1}$ for Fc–Ph(2,3)–(Pc)$_2$ and 960 cm$^{-1}$ for Fc–Ph(2,4)–(Pc)$_2$, respectively (Figure S84).[16] Thus, the electronic coupling systematically decreased with increasing the *n*.

In contrast with the constant mean-plane distance between two Pc units (ca. 3.2–3.4 Å) by DFT, the slipping distances increase with increasing the *n* when viewed perpendicular to the $\pi$-plane of Pc unit (Figures 3, S81). This agrees with the above-mentioned trends of the electronic coupling values. The larger slipping distances should be associated with the torsional trends (i.e., conformational flexibilities) of Fc–Ph(2,*n*)–(Pc)$_2$ because of the decreased steric hinderance between two Pc units (see below) (Figure S82). Thus, Fc–Ph(2,4)–(Pc)$_2$ demonstrated relatively small electronic coupling and large conformational flexibility. This is in sharp contrast with Fc–Ph(2,2)–(Pc)$_2$ with large electronic coupling and small conformational flexibility. These were further discussed by the thermodynamic evaluations using temperature-dependent TA (see below). Then, fluorescence spectra of Pc-dimers were similarly measured in toluene (Figure S85). The significant fluorescence quenching trends of Fc–Ph(2,*n*)–(Pc)$_2$ and Xan–Ph(2,*n*)–(Pc)$_2$ relative to Pc-ref were observed. This is associated with ISF.

To evaluate ISF dynamics, first, TA were performed in toluene. Before measurements, triplet-triplet (T–T) and singlet-singlet (S–S) absorption spectra of Pc-dimers were measured (Figures S86–S91). The S–S absorption of Pc was confirmed by femtosecond transient absorption spectra (fs-TAS) of Pc-ref (Figure S91). The T–T absorption of Pc-dimers were determined by triplet-triplet energy transfer from anthracene (a sensitizer) to Pc-dimers.

fs-TAS of Fc–Ph(2,4)–(Pc)$_2$ and Xan–Ph(2,4)–(Pc)$_2$ are shown in Figure 5 together with the other Pc-dimers such as Fc–Ph(2,2)–(Pc)$_2$, Fc–Ph(2,3)–(Pc)$_2$ and Xan–Ph(2,3)–(Pc)$_2$ (Figures S92–S94). Figures 5A–5B show fs-TAS of Fc–Ph-(2,4)–(Pc)$_2$ and species-associated spectra (SAS) by target analysis, respectively. SAS were obtained by target analysis (see below).[17] After photoexcitation, broad S–S absorption with absorption maxima at ca. 460 and 535 nm immediately appeared together with negative absorption with the ground

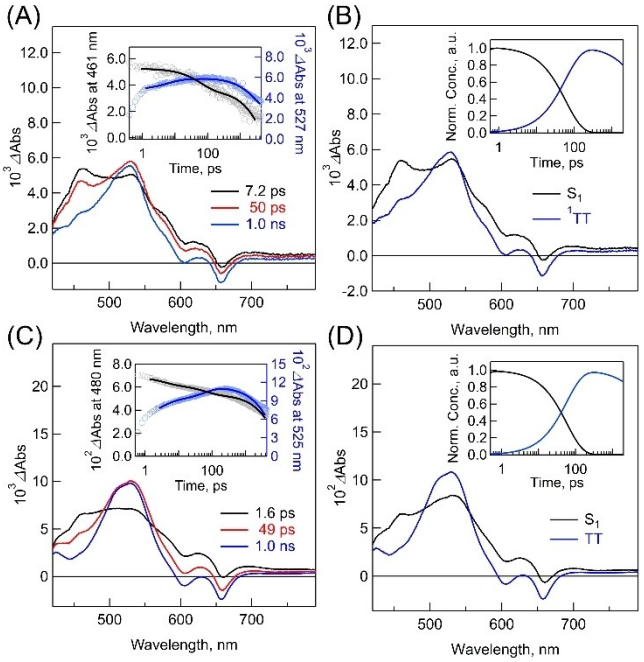


***Figure 5.*** (A) fs-TAS of Fc–Ph(2,4)–$(Pc)_2$ in toluene ($\lambda_{ex}$: 343 nm). The inset figure shows the corresponding time-profiles at 461 and 527 nm. (B) SAS of Fc–Ph(2,4)–$(Pc)_2$. The inset figure shows the time-dependent concentrations of $S_1$ (black) and $^1$TT (blue). (C) fs-TAS of Xan–Ph(2,4)–$(Pc)_2$ in toluene ($\lambda_{ex}$: 343 nm). The inset figure shows the corresponding time-profiles at 480 and 525 nm. (D) SAS of Xan–Ph-(2,4)–$(Pc)_2$. The inset figure shows the time-dependent concentrations of $S_1$ (black) and $^1$TT (blue).

state bleaching at 655 nm. Then, the S–S absorption at 460 nm significantly decreased within ca. 60 ps, whereas the T–T absorption appeared at around 530 nm as shown in the inset Figure (Figure 5A). SAS also demonstrated the $S_1$ decay together with $^1$TT generation. The plausible reason for $^1$TT is discussed below. Such a fast singlet-triplet conversion should be attributed to ISF. Note that there is no competition between ISF and ISC in the present system because of the much larger ISF rate constants. Figures 5C–5D also show fs-TAS of Xan–Ph(2,4)–$(Pc)_2$ and corresponding SAS, respectively. The photophysical trends of Fc–Ph-(2,4)–$(Pc)_2$ are approximately similar to Xan–Ph(2,4)–$(Pc)_2$ in the time region from femtosecond to nanosecond.

To discuss the dynamics, we analyzed SAS based on the proposed kinetic model (Schemes 2, S8). The rate constant for the relaxation process from $S_1$ to ground state ($S_0$) is denoted as $k_0$. Then, ISF from $S_1$ to $^1$TT ($k_{ISF}$), recombination from $^1$TT to the ground state ($k_{1REC}$), spin conversion (SC) from $^1$TT to $^5$TT ($k_{SC}$) and deactivation from $^5$TT to $S_0$ ($k_{5REC}$) are included. In addition, the kinetic constant corresponding to reciprocal of $^1$TT lifetime is denoted as $k_{1TT}$ (i.e., $k_{1TT}=k_{SC}+k_{1REC}$). Then, we analyzed SAS and time-dependent concentration profiles (Figures 5–6, S92–S97). These parameters are summarized in Table 1. The rate constant of $^1$TT generation ($k_{ISF}$) in Fc–Ph(2,4)–$(Pc)_2$ was determined to be $1.6\times10^{10}$ s$^{-1}$. This is quite similar to that in Xan–Ph(2,4)–$(Pc)_2$ ($1.7\times10^{10}$ s$^{-1}$) because of the similar conformation of two Pc chromophores, whereas the $k_{ISF}$ in Fc–Ph(2,2)–$(Pc)_2$ is larger than the above values because of the increased electronic coupling (*vide supra*). These $k_{ISF}$ values were more than two orders of magnitude greater than the $k_0$ (Table 1), which suggested the approximate quantitative $^1$TT generation in all systems ($\Phi_{1TT}$: ≈100 %) (Table 1).

Next, to evaluate SC from $^1$TT to $^5$TT in Pc-dimers, picosecond transient absorption spectra (ps-TAS) were performed in toluene (Figure 6, Figures S95–S97). The discussion on the SC process, rather than TT dissociation, is presented below. Figures 6A–6B show ps-TAS of Fc–Ph-(2,4)–$(Pc)_2$ and SAS together with Xan–Ph(2,4)–$(Pc)_2$ (Figures 6C–6D). The other Pc-dimers such as Fc–Ph(2,2)–$(Pc)_2$, Fc–Ph(2,3)–$(Pc)_2$ and Xan–Ph(2,3)–$(Pc)_2$ are shown in Figures S95–S97. These kinetic parameters are shown in Table 1. In ps-TAS of Fc–Ph(2,4)–$(Pc)_2$, we can initially see a broad absorption signal at around 525 nm derived from

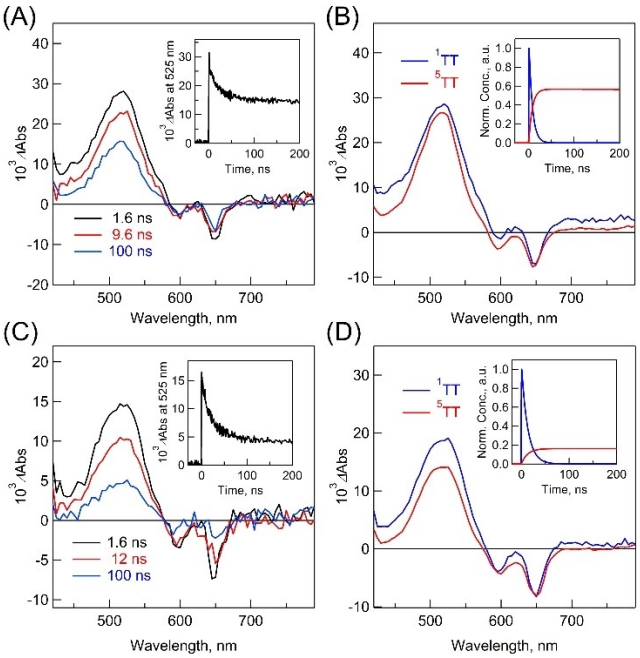


***Figure 6.*** (A) ps-TAS of Fc–Ph(2,4)–$(Pc)_2$ in toluene ($\lambda_{ex}$: 355 nm). The inset figure shows time-profile at 525 nm. (B) SAS of Fc–Ph(2,4)–$(Pc)_2$. The inset figure shows the time-depending concentrations of $^1$TT (blue) and $^5$TT (red). (C) ps-TAS of Xan–Ph(2,4)–$(Pc)_2$ in toluene ($\lambda_{ex}$: 355 nm). The inset figure shows the time-profile at 525 nm. (D) SAS of Xan–Ph(2,4)–$(Pc)_2$. The inset figure shows the time-dependent concentrations of $^1$TT (blue) and $^5$TT (red).

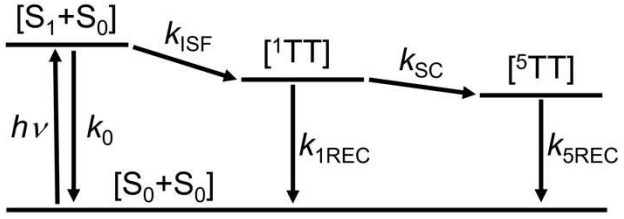


***Scheme 2.*** A Proposed Kinetic Scheme of Pc-Dimers.

***Table 1:*** Summarized Kinetic Parameters.

| | $k_0$[a] ($\times10^8$ $s^{-1}$) | $k_{ISF}$[b] ($\times10^{10}$ $s^{-1}$) | $k_{1REC}$[c] ($\times10^7$ $s^{-1}$) | $k_{SC}$[d] ($\times10^7$ $s^{-1}$) | $k_{SC}/k_{1REC}$ | $k_{5TT}$[e] ($\times10^4$ $s^{-1}$) [$\tau_{5TT}$[e] (μs)] | $\Phi_{1TT}$[f] (%) | $\Phi_{5TT}$[g] (%) |
|---|---|---|---|---|---|---|---|---|
| Fc–Ph(2,2)–$(Pc)_2$ | 4.5 | 1.9 | 21 | 3.1 | 0.14 | 2.8 (36) | 100 | 13 |
| Fc–Ph(2,3)–$(Pc)_2$ | 0.83 | 1.6 | 34 | 12 | 0.35 | 2.8 (36) | 100 | 26 |
| Fc–Ph(2,4)–$(Pc)_2$ | 0.83 | 1.6 | 5.7 | 7.3 | 1.3 | 2.6 (38) | 100 | 55 |
| Xan–Ph(2,3)–$(Pc)_2$ | 0.60 | 1.7 | 9.8 | 0.41 | 0.042 | 3.2 (31) | 100 | 4.0 |
| Xan–Ph(2,4)–$(Pc)_2$ | 0.60 | 1.7 | 6.5 | 1.2 | 0.18 | 3.0 (33) | 100 | 15 |

[a] Estimated by ps-TAS of Pc-ref (Table S3). [b] Estimated by fs-TAS. [c] Calculated by $k_{REC}=k_{1TT}$-$k_{SC}=(\tau_{1TT})^{-1}$-$k_{SC}$. The $\tau_{1TT}$ was estimated by ps-TAS. [d] Calculated by $k_{SC}=k_{1TT}\times\Phi_{5TT}/\Phi_{1TT}$. [e] Calculated by $k_{5TT}=\tau_{5TT}^{-1}$, $\tau_T$ was estimated by ns-TAS. [f] Calculated by SAS of fs-TAS. [g] Estimated by SAS of ps-TAS.

$^1$TT. It then changes to a sharper $^5$TT spectrum with increasing the time. In the inset figure of Figure 6A, we can see two different lifetime components. The faster component should be derived from $^1$TT and the slow component from $^5$TT according to the previous report.[18] Although such a spectral change is similar to the other systems such as Xan–Ph(2,4)–$(Pc)_2$, the major difference concerns the SC.

Therefore, the $^5$TT quantum yield ($\Phi_{5TT}$) can be estimated by SAS. Note that the maximum $\Phi_{5TT}$ is 100 %. Consequently, the $\Phi_{5TT}$ of Fc–Ph(2,4)–$(Pc)_2$ was determined to be 55 %. This is much larger than the other systems such as Xan–Ph(2,4)–$(Pc)_2$ (15 %) and Fc–Ph(2,2)–$(Pc)_2$ (13 %). The much enhanced $\Phi_{5TT}$ can probably be attributed to the larger conformational flexibility in Fc–Ph(2,4)–$(Pc)_2$ during the SC. In Fc–Ph(2,*n*)–$(Pc)_2$, the $\Phi_{5TT}$ values significantly increased with increasing the *n*. Moreover, the relative ratio between $k_{1REC}$ and $k_{SC}$ in Fc–Ph(2,4)–$(Pc)_2$ ($k_{SC}/k_{1REC}=1.3$) is much larger than the other Pc-dimers. This is highly associated with the differences of $\Phi_{5TT}$ values. Additionally, the $^5$TT deactivation rate constants ($k_{5REC}$) of Fc–Ph(2,*n*)–$(Pc)_2$ were calculated from the lifetimes ($\tau_{5TT}$: ≈30 μs) by nanosecond transient absorption spectra (ns-TAS) (Table 1, Figure S98). These species were directly determined to be $^5$TT by TREPR (see below).

To examine the plausible reasons for the enhanced quintet generation of TT in Fc–Ph(2,4)–$(Pc)_2$ relative to the other Pc-dimers, we have further measured the temperature-dependent ps-TAS in toluene ($\lambda_{ex}$: 355 nm) (Figures 7, S99).[11] Increased $\Phi_{5TT}$ values were observed in all Pc-dimers. For example, the $\Phi_{5TT}$ of Fc–Ph(2,4)–$(Pc)_2$ increased up to 63 % at 333 K.

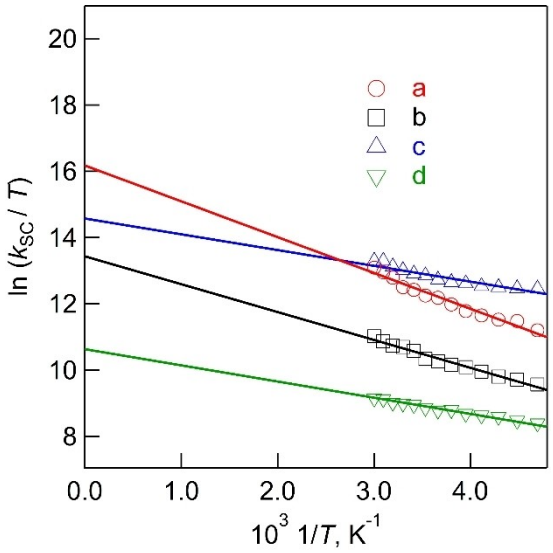


***Figure 7.*** Eyring plots of the SC process ($^1$TT→$^5$TT) in (a) Fc–Ph(2,4)–$(Pc)_2$, (b) Xan–Ph(2,4)–$(Pc)_2$, (c) Fc–Ph(2,3)–$(Pc)_2$ and (d) Xan–Ph-(2,3)–$(Pc)_2$. The fitting function was calculated by the following equation: $[\ln(k_{SC}/T)=-(\Delta H^{\ddagger}/RT)+\ln(k_B/h)+(\Delta S^{\ddagger}/R)]$, where $\Delta H^{\ddagger}$, *R*, *h*, and $\Delta S^{\ddagger}$ are activation enthalpy, gas constant, Planck constant, and activation entropy, respectively.

First, we calculated the pre-exponential factor ($A$) by using Arrhenius plots of $k_{SC}$ (Table 2, Figure S100). These differences of $A$ obtained from the intercepts are associated with activation energies ($E_A$) determined from the slopes of the Arrhenius plots (Table S6), which demonstrate the key role of steric factor. Then, activation enthalpy ($\Delta H^{\ddagger}$), activation entropy ($\Delta S^{\ddagger}$) and Gibbs free energy of activation

***Table 2:*** Thermodynamic Parameters Regarding SC Process ($^1$TT→$^5$TT).

| | $A$[a] ($\times10^8$ $s^{-1}$) | $\Delta H^{\ddagger}$[b] (kJ $mol^{-1}$) | $\Delta S^{\ddagger}$[c] (J $mol^{-1}$ $K^{-1}$) | $-T\triangle S^{\ddagger}$ at 298 K[c] (kJ $mol^{-1}$) | $\triangle G^{\ddagger}$ at 298 K[d] (kJ $mol^{-1}$) |
|---|---|---|---|---|---|
| Fc–Ph(2,2)–$(Pc)_2$ | 1.42 | 1.24 ± 0.02 | −96.2 ± 0.96 | 28.7 | 29.9 |
| Fc–Ph(2,3)–$(Pc)_2$ | 12.2 | 3.96 ± 0.06 | −76.4 ± 1.2 | 22.8 | 26.7 |
| Fc–Ph(2,4)–$(Pc)_2$ | 48.8 | 8.99 ± 0.49 | −63.0 ± 1.0 | 18.8 | 27.8 |
| Xan–Ph(2,3)–$(Pc)_2$ | 0.45 | 4.06 ± 0.02 | −109 ± 0.61 | 32.5 | 36.6 |
| Xan–Ph(2,4)–$(Pc)_2$ | 4.95 | 7.98 ± 0.31 | −83.1 ± 0.80 | 24.7 | 32.7 |

[a] Estimated by Arrhenius plot (Figure S100). [b] Estimated by Eyring plot (Figures 6B, S101). The standard errors in $\Delta S^{\ddagger}$ were less than ±1 J $mol^{-1}$ $K^{-1}$ from the least-squares fitting. [c] Calculated by $-T\triangle S^{\ddagger}=-298(K)\times\triangle S^{\ddagger}$. [d] Calculated by $\triangle G^{\ddagger}=\triangle H^{\ddagger}-T\times\triangle S^{\ddagger}=\triangle H^{\ddagger}-298(K)\times\triangle S^{\ddagger}$.

($\Delta G^{\ddagger}$) from $^{1}$TT state to the transition state (‡) were estimated by using the Eyring plots (Figures 7, S101, Table S7). This is met at temperatures higher than 200 K, where the low-frequency modes are primarily involved in promoting various conformational motions.[10a] The values of $\Delta H^{\ddagger}$ and $\Delta S^{\ddagger}$ were consequently calculated from the slopes and intercepts, respectively (Table 2). The plots of $\Delta S^{\ddagger}$ versus $\Delta H^{\ddagger}$ showed that a linear correlation in Fc–Ph(2,*n*)–$(Pc)_2$, and the enthalpy-entropy compensation effect was successfully observed (Figure S102). The relatively large $\Delta S^{\ddagger}$ of Fc–Ph(2,4)–$(Pc)_2$ are highly associated with the rotational flexibility of Fc (conformation flexibility) as discussed above and will be detailed below.[10a]

Then, we focused on the presence and absence of the rotational units such as Fc–Ph(2,*n*)–$(Pc)_2$ and Xan–Ph(2,*n*)–$(Pc)_2$. For example, similar $\Delta H^{\ddagger}$ values were observed in the case of Fc–Ph(2,3)–$(Pc)_2$ (3.96 $kJ^{-1}mol^{-1}$) and Xan–Ph(2,3)–$(Pc)_2$ (4.06 $kJ^{-1}mol^{-1}$]. There is also a quite similar difference between Fc–Ph(2,4)–$(Pc)_2$ (8.99 $kJ^{-1}$) and Xan–Ph(2,4)–$(Pc)_2$ (7.98 $kJ^{-1}mol^{-1}$). Therefore, $\Delta H^{\ddagger}$ is probably related to the orientation between two Pc-chromophores in $^{1}$TT. Then, the $\Delta S^{\ddagger}$ of Fc–Ph(2,4)–$(Pc)_2$ ($-63.0$ $kJ^{-1}mol^{-1}$) is larger than those in Fc–Ph(2,3)–$(Pc)_2$ ($-76.4$ $kJ^{-1}mol^{-1}$) and Xan–Ph(2,4)–$(Pc)_2$ ($-83.1$ $kJ^{-1}mol^{-1}$), whereas the $\Delta S^{\ddagger}$ of Xan–Ph(2,3)–$(Pc)_2$ ($-109$ $kJ^{-1}mol^{-1}$) is smaller than those of Fc–Ph(2,3)–$(Pc)_2$ and Xan–Ph(2,4)–$(Pc)_2$. Such differences in these values agree with the $\Phi_{5TT}$ values such as Fc–Ph(2,4)–$(Pc)_2$ ($\Phi_{5TT}$: 55 %) and Xan–Ph(2,3)–$(Pc)_2$ ($\Phi_{5TT}$: 4.0 %). Since the $\Phi_{5TT}$ values depend on the ratio of $k_{SC}$ and $k_{1REC}$ ($k_{SC}/k_{1REC}$), we can conclude the $\Delta S^{\ddagger}$ is associated with the conformation flexibilities. This clearly indicated that the flexible Fc linker induced the large conformational change associated with the motion of Fc relative to Xan. Moreover, the $\Delta S^{\ddagger}$ of Fc–Ph(2,4)–$(Pc)_2$ is about 20 $J\,mol^{-1}\,K^{-1}$ larger than that of Xan–Ph(2,4)–$(Pc)_2$. Considering the Boltzmann's formula, the following equations (eqs(2)–(3)) were obtained ($W$: number of states, $k_B$: Boltzmann's constant).

$$\Delta S = k_B \ln\{W(\text{Fc–Ph(2,4)–(Pc)}_2)\} - k_B \ln\{W(\text{Xan–Ph(2,4)–(Pc)}_2)\} \quad (2)$$

$$\Delta W = W(\text{Fc–Ph(2,4)–(Pc)}_2)/W(\text{Xan–Ph(2,4)–(Pc)}_2) \quad (3)$$

Here $\Delta S$ represents the activation entropy difference between Fc–Ph(2,4)–$(Pc)_2$ and Xan–Ph(2,4)–$(Pc)_2$ for the SC from $^{1}$TT to $^{5}$TT. Thus, $\Delta W$ denotes the difference in the density of states in the activated $^{1}$TT, possibly caused by disorder in $^{1}$TT conformations. $\Delta W \approx 20$ was calculated. In $^{1}$TT states, the number of states consequently increased by a factor of $\Delta W = \approx 20$ because Fc became more flexible due to the reduced binding properties (see below).

Additionally, the following trend was observed when comparing $-T\triangle S^{\ddagger}$ at 298 K (Table 2). It should be emphasized that the values of $-T\triangle S^{\ddagger}$ are an order of magnitude greater than those of $\Delta H^{\ddagger}$ in all Pc-dimers. This result indicated that the low-frequency vibrational motion of frequency $\nu$ ($h\nu \ll k_B T$) play a major role on the thermal activation ($\Delta H^{\ddagger} \approx RT$) of breaking the T–T binding enthalpy to weaken the electronic bonds for generating $^{5}$TT as discussed in our previous reports.[10a,11]

Finally, we estimated the $\triangle G^{\ddagger}$ values at 298 K by using the above-mentioned values such as $\Delta H^{\ddagger}$ and $-T\Delta S^{\ddagger}$. The smaller $\triangle G^{\ddagger}$ value of Fc–Ph(2,3)–$(Pc)_2$ [26.7 $kJ\,mol^{-1}$] relative to Xan–Ph(2,3)–$(Pc)_2$ [36.6 $kJ\,mol^{-1}$] is similar to Fc–Ph(2,4)–$(Pc)_2$ [27.8 $kJ\,mol^{-1}$] relative to Xan–Ph(2,4)–$(Pc)_2$ [32.4 $kJ\,mol^{-1}$]. Additionally, the $\triangle G^{\ddagger}$ value of Fc–Ph(2,4)–$(Pc)_2$ is slightly larger than that of Fc–Ph(2,3)–$(Pc)_2$. This trend is probably associated with that in $k_{SC}$ values. Based on the above, we can summarize that Fc–Ph(2,4)–$(Pc)_2$ has largest conformational flexibility for efficient SC.

To exactly assign the spin states (i.e., $^{1}$TT and $^{5}$TT) and to understand molecular motions responsible for the quintet, TREPR was performed on Fc–Ph(2,4)–$(Pc)_2$ (Figure 8) at room temperature. Importantly, the quintet EPR signal was confirmed in toluene/paraffin mixture (1/9, v/v) with the 656 nm excitation. The absorptive (A) spin polarization for $t = 0.1$ μs is explained by anisotropic singlet-quintet conversion (red-lines in Figure 8) during a quick conformational dynamics (frequency = 3.3 $cm^{-1}$) between stabilized quintet state of $TT_1$ and activated state ($TT_2$) with $^{5}TT_{m_S=2,1,0,-1,-2}$ via the quintet-singlet (Q–S) interconversion from $TT_2$ (Figure 9). The emissive (E) quintet spectrum in Figure 8B for $t > 0.5$ μs is successfully computed using the above vibronic spin model with setting minor initial equal sublevel populations in the quintet as, $\rho_{Q2,Q2} = \rho_{Q+1,Q+1} = \rho_{Q0,Q0} = \rho_{Q-1,Q-1} = \rho_{Q-2,Q-2} = 0.02$, while $\rho_{S,S} = 1$ in $^{1}TT_1$ at $t = 0.0$ μs (Table S8).

Thus, the quick spin relaxation after ISF in TT is revealed for reverse Q–S conversions to obtain the emissive spin polarization via the singlet deactivation. The present quick spin relaxation and conformation dynamics are very consistent with the large $\Delta S^{\ddagger}$ in Table 2 causing the modulation of the spin-spin interactions in Fc–Ph(2,4)–$(Pc)_2$. This relaxation dynamics is supported by absence of

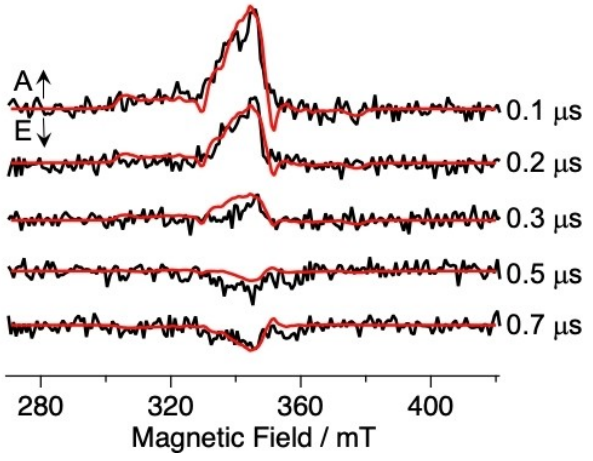


***Figure 8.*** Delay time-dependence of TREPR spectra of Fc–Ph(2,4)–$(Pc)_2$ obtained by the depolarized 656 nm irradiation (0.3 mJ/pulse, 10 Hz) at 298 K of diluted solution (20 μM) in toluene/paraffin mixture (1/9, v/v). Computed spin-polarized $^{5}$TT spectra are shown by the red lines using vibronic spin model (Figure 9) as the function of the delay time.

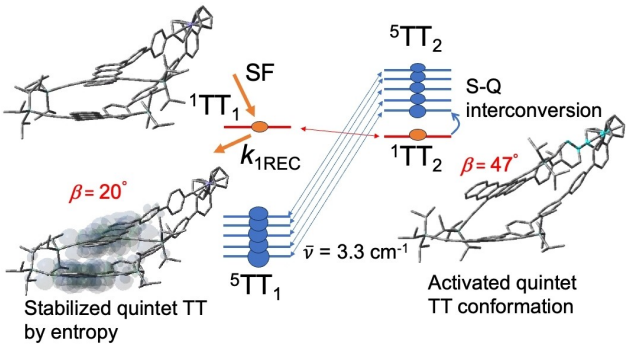


***Figure 9.*** Schematic representation of the electron spin polarization in $^5$TT (Figure 8) after ISF. Time-dependence of the anisotropic quintet sublevel populations are computed by the density matrix formalism analysis considering conformation dynamics of the multiexciton between $TT_1$ and $TT_2$ caused by low-frequency torsional motion in phenylene and Fc bridges.

spin echo signal by the pulsed EPR measurement (Figure S103). We also performed TREPR measurements of Xan–Ph(2,4)–$(Pc)_2$ in toluene/paraffin mixture (1/9, v/v) at room temperature (Figure S104). The absorptive spin polarized spectra around 340 mT are very consistent with the data in Figure 8 observed in Fc–Ph(2,4)–$(Pc)_2$ and with the center absorptive spin polarization of $^5$TT observed in our previous report in a dimer in toluene/paraffin mixture (1/9, v/v) at room temperature.[10b]

On the right side of Scheme in Figure 9, dimer conformation in the activated $TT_2$ is depicted from the dihedral angle ($\beta_2 = 47^\circ$ in Table S8, Figure S105) between the aromatic planes of a triplet exciton ($T_A$) and of the other exciton ($T_B$). We also calculated an optimized molecular geometry ($\beta_1 = 20^\circ$) of the quintet state in this dimer by DFT, as shown in the left of Figure 9. The parallel TT conformation is also preferential in the quintet state, suggesting that significant orbital overlap between $T_A$ and $T_B$ in the dimer causes spin-spin exchange coupling in the quintet spin state, while $^1$TT is subject to the quick recombination ($k_{1REC}$).[19] The positive singlet-quintet (S–Q) gap in the present exciton pair is consistent with the long-lived quintet transient states, as long-lived triplet excitons are usually generated after ISC from the $S_1$ due to the positive $S_1$–$T_1$ gaps. On the other hand, negative S–Q gap is anticipated at the activated conformation for the absorptive spin polarization by $^1TT \rightarrow {}^5TT_{m_S \le 0}$ interconversion at the weakened exchange-coupling ($J < 0$)[15] (Figure 9). The emissive spin polarization at the later delay time is thus explained by the preferential $^5TT_{m_S \le 0} \rightarrow {}^1TT$ back-conversion and subsequent singlet deactivation with $k_{1REC}$: 73 μs$^{-1}$. The positive S–Q gap (Figure 9 left) is rationalized by the entropy gain for the quintet generation using DFT (Table S10).

The dimer conformation with $\beta = 47^\circ$ in the activated $TT_2$ of Figure 9 can be obtained by torsional motion of the phenylene-phenylene (Ph–Ph) and the Ph–Fc dihedral angles in the linker from these of the stabilized quintet conformer. The large $\Delta H^\ddagger$ in Fc–Ph(2,4)–$(Pc)_2$ suggests that the steric barrier is large on the activation in the excited state. This is consistent with a sterically hindered structure by the bulky TIPS-substituent in Figure 9, strongly supporting the vibronic spin model to reproduce the electron spin polarization in Figures 8, S105. Furthermore, lack of the EPR signals by $^3$TT and $T_1 + S_0$ pair states denotes that the triplet-triplet annihilation (TTA) by $^5TT \rightarrow {}^3TT \rightarrow T_1 + S_0$ is minor in the present parallel TT conformations (Figure 1).[10c,20]

To confirm the TREPR results, TA of Fc–Ph(2,4)–$(Pc)_2$ were performed in toluene/paraffin mixture at 298 K (Figures S106–S108). We observed the efficient ISF although with the slight decrease of the $\Phi_{5TT}$ (45 %) (Table S9). Such a decrease should be ascribed to the increased solvent viscosity, which partially suppressed the conformational change during the SC and allowed the reverse process ($k_{rSC}$) from $^5$TT into $^1$TT for the emissive polarization in Figure 8. Then, we performed target analysis based on the newly proposed kinetic scheme considering the $k_{rSC}$ values (Scheme S9, Tables S9–S10). The rate constant of the SC obtained from TA were in good agreement with those simulated from room-temperature TREPR (Figure 8).

Based upon the above experimental findings we examined the ns-spin conversion mechanism in TT. For this we have calculated the electronic structure of the excited triplet state of Fc–Ph(2)–Pc (Figure 10) at the optimized geometry by DFT. The spin density is partially delocalized to the Ph–Ph and Ph–Fc units in the linker (Figure 10A) and is consistent with the extended highest occupied natural transition orbital (HONTO: 260α) in Figure 10B, while such hybridization is not significant in the lowest unoccupied natural transition orbital (LUNTO: 261α) in Figure 10C. This is highly associated with the electrochemical results because the oxidation potential of Fc in Fc–Ph(2)–Pc is positively shifted as compared to pristine Fc (Figures S109–S112, Table S11). The hybridization of the hole with the Ph–Ph and Ph–Fc antibonding orbital (Figure 10B) of the

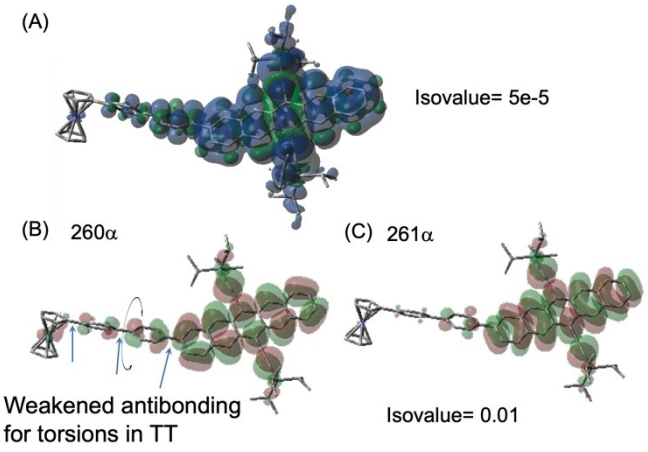


***Figure 10.*** (A) Spin density distribution of the triplet exciton in Fc–Ph-(2)–Pc for an optimized geometry by using UB3LYP/6–31G(d,p) level of theory. (B) and (C) represent natural transition orbitals of 260α and 261α in the triplet exciton, respectively, showing hybridization of the hole level of Pc to Fc.

triplet exciton simply means that the Ph–Ph and Ph–Fc bonds are strengthened by the removal of the electron from this orbital in TT.[10c] Therefore, the reasons for the torsional motion in TT should be attributable to the hybridization of the hole level of Pc to Fc in TT to strengthen the Pc–Ph–Ph–Fc bonding (Figure 10B): the large activated entropy $\Delta S^{\ddagger}$ and $\Delta W \approx 20$ in eq.(3) of Fc–Ph(2,4)–$(Pc)_2$ relative to Xan–Ph(2,4)–$(Pc)_2$ (Figure 10B), resulting in the twenty-fold disorder in the activated TT conformations (Figure S105 A), as associated with the low-frequency rotational behavior of chromophores (Figure 9).

## Conclusion

In summary, a series of Fc–Ph(2,*n*)–$(Pc)_2$ were synthesized to examine the torsional motion effect of linkers on the ISF dynamics. Fc–Ph(2,4)–$(Pc)_2$ exhibits efficient $\Phi_{5TT}$: 55 % at 298 K (63 % at 333 K) together with quantitative $^1$TT generation. In thermodynamic evaluations of SC, Fc–Ph-(2,4)–$(Pc)_2$ demonstrated the largest activation entropy ($\triangle S^{\ddagger}$) compared to the other systems due to the larger conformational change. This demonstrates the close relationship between $\Phi_{5TT}$ and the structural flexibility associated with the torsional motion at the linkers enhances the number of states in the activated $TT_2$, contributing to the efficient $^1$TT activation for the largest positive activation enthalpy to be overcame in Fc–Ph(2,*n*)–$(Pc)_2$ as confirmed by TREPR. The SF-induced E-polarization via the singlet TTA is rationalized for the first time to be originating from the singlet deactivation in the presence of the exchange coupling after the quick spin-relaxation by the conformation dynamics. The large degree of the torsional motion at the activation is attributable to hybridization of the hole level of Pc to Ph–Ph–Fc unit in TT. In addition to the activations, we can reasonably conclude that this hybridization in $^5$TT also causes the entropy gains for the long-lived strongly coupled multiexciton in the quintet characters. These will provide a new perspective for the future development of photovoltaic and magnetic switching devices.

## Acknowledgements

This work was partially supported by JSPS KAKENHI Grant-in-Aid for Transformative Research Areas, "Dynamic Exciton" (JP20H05832 to Y.K., JP20H05839 to M.H., JP21H05403 to T.H.), "Materials Science of Meso-Hierarchy" (JP23H04876 to T. H.) and Grant Nos. JP20K05652, JP23K04708 to H.S., JP19H00888, JP20K21174 to Y.K, JP20H05234, JP20KK0120, JP21H01908, JP21K19011, 22H04558 to T.H., JST-CREST Program (JPMJCR23I6) to Y.K. This work was partially carried out by the joint research program of Molecular Photoscience Research Center, Kobe University and the Research Program of "Five-star Alliance" in "NJRC Mater. & Dev.".

## Conflict of Interest

The authors declare no conflict of interest.

## Data Availability Statement

The data that support the findings of this study are available in the supplementary material of this article.

**Keywords:** Ferrocene · Multiexciton Formation · Pentacene · Rotational Motion · Singlet Fission

[1] a) H. Noji, R. Yasuda, M. Yoshida, K. Kinosita, *Nature* **1997**, *386*, 299–302; b) M. Schliwa, G. Woehlke, *Nature* **2003**, *422*, 759–765.
[2] a) G. S. Kottas, L. I. Clarke, D. Horinek, J. Michl, *Chem. Rev.* **2005**, *105*, 1281–1376; b) N. Koumura, R. W. J. Zijlstra, R. A. van Delden, N. Harada, B. L. Feringa, *Nature* **1999**, *401*, 152–155; c) S. P. Fletcher, F. Dumur, M. M. Pollard, B. L. Feringa, *Science* **2005**, *310*, 80–82.
[3] a) E. W. Abel, N. J. Long, K. G. Orrell, A. G. Osborne, V. Šik, *J. Organomet. Chem.* **1991**, *403*, 195–208; b) S. O. Scottwell, J. D. Crowley, *Chem. Commun.* **2016**, *52*, 2451–2464.
[4] a) T. Muraoka, K. Kinbara, Y. Kobayashi, T. Aida, *J. Am. Chem. Soc.* **2003**, *125*, 5612–5613; b) T. Muraoka, K. Kinbara, T. Aida, *Nature* **2006**, *440*, 512–515.
[5] a) J. D. Crowley, I. M. Steele, B. Bosnich, *Chem. Eur. J.* **2006**, *12*, 8935–8951; b) A. Iordache, M. Oltean, A. Milet, F. Thomas, B. Baptiste, E. Saint-Aman, C. Bucher, *J. Am. Chem. Soc.* **2012**, *134*, 2653–2671; c) A. Takai, T. Yasuda, T. Ishizuka, T. Kojima, M. Takeuchi, *Angew. Chem. Int. Ed.* **2013**, *52*, 9167–9171.
[6] a) S. O. Scottwell, A. B. Elliott, K. J. Shaffer, A. Nafady, C. J. McAdam, K. C. Gordon, J. D. Crowley, *Chem. Commun.* **2015**, *51*, 8161–8164; b) S. O. Scottwell, J. E. Barnsley, C. J. McAdam, K. C. Gordon, J. D. Crowley, *Chem. Commun.* **2017**, *53*, 7628–7631; c) T. Ikeda, S. Shinkai, K. Sada, M. Takeuchi, *Tetrahedron Lett.* **2009**, *50*, 2006–2009; d) A. Takai, T. Kajitani, T. Fukushima, K. Kishikawa, T. Yasuda, M. Takeuchi, *J. Am. Chem. Soc.* **2016**, *138*, 11245–11253.
[7] a) K. Miyata, F. S. Conrad-Burton, F. L. Geyer, X. Y. Zhu, *Chem. Rev.* **2019**, *119*, 4261–4292; b) M. B. Smith, J. Michl, *Chem. Rev.* **2010**, *110*, 6891–6936.
[8] S. R. Yost, J. Lee, W. B. WilsonMark, T. Wu, D. P. McMahon, R. R. Parkhurst, N. J. Thompson, D. N. Congreve, A. Rao, K. Johnson, M. Y. Sfeir, M. G. Bawendi, T. M. Swager, R. H. Friend, M. A. Baldo, T. Van Voorhis, *Nat. Chem.* **2014**, *6*, 492–497.
[9] a) J. Zirzlmeier, D. Lehnherr, P. B. Coto, E. T. Chernick, R. Casillas, B. S. Basel, M. Thoss, R. R. Tykwinski, D. M. Guldi, *Proc. Natl. Acad. Sci. USA* **2015**, *112*, 5325–5330; b) E. G. Fuemmeler, S. N. Sanders, A. B. Pun, E. Kumarasamy, T. Zeng, K. Miyata, M. L. Steigerwald, X. Y. Zhu, M. Y. Sfeir, L. M. Campos, N. Ananth, *ACS Cent. Sci.* **2016**, *2*, 316–324; c) T. Sakuma, H. Sakai, Y. Araki, T. Mori, T. Wada, N. V. Tkachenko, T. Hasobe, *J. Phys. Chem. A* **2016**, *120*, 1867–1875; d) H. Sakai, R. Inaya, H. Nagashima, S. Nakamura, Y. Kobori, N. V. Tkachenko, T. Hasobe, *J. Phys. Chem. Lett.* **2018**, *9*, 3354–3360; e) B. S. Basel, C. Hetzer, J. Zirzlmeier, D. Thiel, R. Guldi, F. Hampel, A. Kahnt, T. Clark, D. M. Guldi, R. R. Tykwinski, *Chem. Sci.* **2019**, *10*, 3854–3863; f) R. Ringström, F. Edhborg, Z. W. Schroeder, L. Chen, M. J. Ferguson, R. R. Tykwinski, B. Albinsson, *Chem. Sci.* **2022**, *13*, 4944–4954;

g) N. V. Korovina, N. F. Pompetti, J. C. Johnson, *J. Chem. Phys.* **2020**, *152*, 040904; h) S. Lukman, K. Chen, J. M. Hodgkiss, D. H. P. Turban, N. D. M. Hine, S. Dong, J. Wu, N. C. Greenham, A. J. Musser, *Nat. Commun.* **2016**, *7*, 13622; i) R. M. Young, M. R. Wasielewski, *Acc. Chem. Res.* **2020**, *53*, 1957–1968; j) N. V. Korovina, C. H. Chang, J. C. Johnson, *Nat. Chem.* **2020**, *12*, 391–398; k) A. T. Gilligan, E. G. Miller, T. Sammakia, N. H. Damrauer, *J. Am. Chem. Soc.* **2019**, *141*, 5961–5971; l) N. Alagna, J. Han, N. Wollscheid, J. L. P. Lustres, J. Herz, S. Hahn, S. Koser, F. Paulus, U. H. F. Bunz, A. Dreuw, T. Buckup, M. Motzkus, *J. Am. Chem. Soc.* **2019**, *141*, 8834–8845.

[10] a) Y. Kobori, M. Fuki, S. Nakamura, T. Hasobe, *J. Phys. Chem. B* **2020**, *124*, 9411–9419; b) S. Nakamura, H. Sakai, H. Nagashima, M. Fuki, K. Onishi, R. Khan, Y. Kobori, N. V. Tkachenko, T. Hasobe, *J. Phys. Chem. C* **2021**, *125*, 18287–18296; c) T. Hasobe, S. Nakamura, N. V. Tkachenko, Y. Kobori, *ACS Energy Lett.* **2022**, *7*, 390–400; d) S. Nakamura, H. Sakai, M. Fuki, R. Ooie, F. Ishiwari, A. Saeki, N. V. Tkachenko, Y. Kobori, T. Hasobe, *Angew. Chem. Int. Ed.* **2023**, *62*, e202217704.

[11] S. Nakamura, H. Sakai, M. Fuki, Y. Kobori, N. V. Tkachenko, T. Hasobe, *J. Phys. Chem. Lett.* **2021**, *12*, 6457–6463.

[12] A. B. Pun, A. Asadpoordarvish, E. Kumarasamy, M. J. Y. Tayebjee, D. Niesner, D. R. McCamey, S. N. Sanders, L. M. Campos, M. Y. Sfeir, *Nat. Chem.* **2019**, *11*, 821–828.

[13] D. N. Congreve, J. Lee, N. J. Thompson, E. Hontz, S. R. Yost, P. D. Reusswig, M. E. Bahlke, S. Reineke, T. Van Voorhis, M. A. Baldo, *Science* **2013**, *340*, 334–337.

[14] T. S. C. MacDonald, M. J. Y. Tayebjee, M. I. Collins, E. Kumarasamy, S. N. Sanders, M. Y. Sfeir, L. M. Campos, D. R. McCamey, *J. Am. Chem. Soc.* **2023**, *145*, 15275–15283.

[15] a) R. M. Jacobberger, Y. Qiu, M. L. Williams, M. D. Krzyaniak, M. R. Wasielewski, *J. Am. Chem. Soc.* **2022**, *144*, 2276–2283; b) S. Matsuda, S. Oyama, Y. Kobori, *Chem. Sci.* **2020**, *11*, 2934–2942.

[16] H. Horinouchi, H. Sakai, Y. Araki, T. Sakanoue, T. Takenobu, T. Wada, N. V. Tkachenko, T. Hasobe, *Chem. Eur. J.* **2016**, *22*, 9631–9641.

[17] a) J. J. Snellenburg, S. Laptenok, R. Seger, K. M. Mullen, I. H. M. van Stokkum, *J. Stat. Software* **2012**, *49*, 1–22; b) I. H. M. van Stokkum, D. S. Larsen, R. van Grondelle, *Biochim. Biophys. Acta Bioenerg.* **2004**, *1657*, 82–104.

[18] B. S. Basel, J. Zirzlmeier, C. Hetzer, B. T. Phelan, M. D. Krzyaniak, S. R. Reddy, P. B. Coto, N. E. Horwitz, R. M. Young, F. J. White, F. Hampel, T. Clark, M. Thoss, R. R. Tykwinski, M. R. Wasielewski, D. M. Guldi, *Nat. Commun.* **2017**, *8*, 15171.

[19] R. D. Dill, K. E. Smyser, B. K. Rugg, N. H. Damrauer, J. D. Eaves, *Nat. Commun.* **2023**, *14*, 1180.

[20] Y. Kawashima, T. Hamachi, A. Yamauchi, K. Nishimura, Y. Nakashima, S. Fujiwara, N. Kimizuka, T. Ryu, T. Tamura, M. Saigo, K. Onda, S. Sato, Y. Kobori, K. Tateishi, T. Uesaka, G. Watanabe, K. Miyata, N. Yanai, *Nat. Commun.* **2023**, *14*, 1056.

Manuscript received: October 18, 2023
Accepted manuscript online: January 5, 2024
Version of record online: January 18, 2024